ADVANCED ENGINEERING MATERIALS
www.aem-journal.com

The Effect of the Deposition Strategy and Heat Treatment on Cold Spray Additive Manufactured 316L Stainless Steel

Rodolpho F. Vaz, Vladimir Luzin, Filomena Salvemini, Giovani G. Ribamar, Julian A. Ávila, Vicente Albaladejo, Javier Sanchez, and Irene Garcia Cano*

Herein, the effect of heat treatment on the characteristics and properties of cold spray additive manufactured 316L stainless steel employing traditional and a new metal knitting strategy is investigated. 316L feedstock powder characteristics, the geometry of the bulk, microstructure, porosity, microhardness, mechanical isotropy, and residual stress are analyzed in both strategies in as-sprayed and heat-treated conditions. Results show that the traditional deposition strategy produced higher mechanical resistance, whereas metal knitting presents a better part geometry accuracy. The heat treatment significantly improves the material strength and the quality of the parts by recovery and recrystallization phenomena. The same microhardness and planar isotropy are achieved after heat treatment of samples produced by both strategies. A discussion about the mechanisms, microstructural, and residual stress evolution is presented.

1. Introduction

Cold spray (CS) is a solid-state deposition, accelerating particles to high velocities onto a surface, bonding by severe plastic deformation. This process was developed as a coating technique; however, it has evolved into an additive manufacturing alternative in recent years, called cold spray additive manufacturing (CSAM). This process can fabricate components with different compositions, such as Ti,[1,2] Al,[3,4] steel,[5] and Cu alloys.[6,7] Compared to other additive manufacturing (AM) processes, one of its main advantages is its capacity to process alloy systems prohibited in fusion processes, such as metal matrix composites or materials with different fusion points, which is possible for CSAM, avoiding the high-temperature harmful effects on the material resulting from its melting and rapid solidification, such as the coarse columnar grains,[8] high tensile residual stress,[9,10] and feedstock material oxidation.[11,12]

However, CSAM parts using the conventional or traditional deposition strategy present difficulties in fabricating high-height thin walls or vertical sidewall parts, requiring additional layers with inclined CS gun for rectifying the sidewall inclination.[1,13,14] Alternatively, and in an attempt to avoid this issue, CSAM Metal Mnitting strategy has been developed in previous works.[15,16] This alternative strategy impresses a circular-like movement on the substrate plane, keeping the CS powder-laden jet not perpendicular to this substrate and describing the final path as a virtual frustum of a cone. This strategy produced thin vertical sidewall parts and large bulks of Ti, Cu, 316L, Ti6Al4V, and Al.[15,16] Despite this advantage, there are few studies on the microstructure developed, and this work increases the knowledge on using CSAM metal knitting for 316L stainless steel.

Among the factors involving AM component quality, the morphology, size, and distribution of pores in the CSAM-ed material are key indicators. Pores can be characterized using different characterization techniques and the influence of building strategy on their development is crucial for validating the proposed strategy. In this sense, neutron tomography (NT) has been used to exploit the interaction between matter and neutron radiation to obtain a spatially resolved map of a specimen or phenomenon,[17] showing how the pores are distributed over the material.

Another important factor involving AM processes is the residual stresses (RS) generated during the material consolidation, cooling time, or post-processing, such as sawing, machining,

R. F. Vaz, V. Albaladejo, J. Sanchez, I. G. Cano
Thermal Spray Centre (CPT)
Department of Materials Science and Chemistry Physics
Universitat de Barcelona
Carrer de Martí i Franquès 1, 08028 Barcelona, Spain
E-mail: rvaz@cptub.eu

V. Luzin, F. Salvemini
Australian Nuclear Science and Technology Organisation
New Illawara Road, Lucas Heights 2232, NSW, Australia

V. Luzin
School of Engineering
The University of Newcastle
University Drive, Callaghan 2308, NSW, Australia

G. G. Ribamar
Department of Metallurgical and Materials Engineering
University of São Paulo
Av. Prof. Mello Moraes, 2463, São Paulo 05508-030, SP, Brazil

J. A. Ávila
Research Group in Structures and Mechanics of Materials (REMM)
Department of Strength of Materials and Structural Engineering
Universitat Politècnica de Catalunya (UPC)
Av. Diagonal 647, 08028 Barcelona, Spain

The ORCID identification number(s) for the author(s) of this article can be found under https://doi.org/10.1002/adem.202302156.

DOI: 10.1002/adem.202302156

heat treatments, or surface finishing.[9] RS affects the intensity and distribution of stresses in a component, producing geometrical distortions or exacerbating the stress concentrators, therefore reducing their mechanical strength. For CSAM, some works by Luzin and co-authors[18–20] concluded that RS is highly correlated with the deformation properties of the material, suggesting that the kinetic effects have more importance than the thermal effects. However, a high mismatch between the coefficient of thermal expansion of the materials, such as Ti and Cu, can result in tensile RS instead of the typical compressive RS presented in the literature for CSAM-ed materials.[21,22]

In order to overcome these issues, post-heat treatments (HT) are normally applied to AM components.[23] It has been reported that in wire arc additive manufactured (WAAM) components of 316L, the δ-ferrite served as the nucleus for the deleterious σ-phase at the annealing at 950 °C per 2 h.[23] However, annealing at 1050 °C promoted the δ-ferrite dissolution and homogenization of the microstructures. For the case of CSAM 316L, the annealing also aids in reducing the porosity volume, where the higher the temperature between 250 and 800 °C, the more porosity reduction.[24,25] In contrast, between 800 and 1100 °C some interesting phenomena occur: i) the porosity reduction tends to stabilize; ii) there is partial or total recrystallization; and iii) the grain size grows, mainly at 1100 °C.[25,26] Concerning mechanical properties, the annealing at 1000 °C presented the highest ultimate tensile strength (UTS), 500 MPa with a 15% elongation to fracture. In comparison, the annealing at 1100 °C depicted a UTS of 400 MPa and elongation of 27%.[25]

In this sense, this work assesses the effects of a HT applied on CSAM 316L components fabricated by two different methods: traditional and Metal Knitting scan strategy, analyzing microstructure, hardness, RS, and mechanical behavior. The results of this work provide scholars with a benchmark study evaluating the three-dimensional distribution and size of porosity produced by different CSAM deposition strategies and the HT effect on CSAM 316L samples. This work helps the CSAM users to select the best deposition strategy based on the higher geometrical accuracy obtained by the metal knitting strategy or on the higher as-sprayed material properties given by the traditional one. In addition, this work presents the HT effectiveness in improving the cohesion of particles and its effect on CSAM 316L properties.

2. Experimental Section

2.1. Feedstock Powder

The feedstock powder was water-atomized Daye 316L stainless steel, selected among others after a previous study evaluating its good performance over gas-atomized ones.[27] Laser scattering measured the powder size distribution in a Beckman Coulter LS13320 equipment in dry mode. Its shape and microstructure were obtained by scanning electron microscopy (SEM) after etching in aqua regia solution. SEM images and particle size distribution are added as Supplementary Material. Inductively coupled plasma was used to analyze the powder nominal composition using a Perkin Elmer Optima ICP-OES 3200 RL equipment.

2.2. CSAM Deposition

A Plasma Giken PCS 100 fitted with a long glass nozzle was used for the part production, operating with N_2 working gas at a pressure of 6 MPa, temperature of 1000 °C, standoff distance of 25 mm, and powder feeding of 0.43 g s^{-1}. Before the deposition, at this standoff distance, the velocity and size of sprayed particles were measured by Oseir HiWatch equipment. The results are presented in Figure C, Supporting Information. The substrate was a 3 mm-thick Al plate previously sand-blasted with alumina to clean and prepare the substrate for thermal spraying.[28]

Traditional scanning strategy consists of moving the gun following a zigzag in each layer, keeping the powder-laden jet perpendicular to the substrate surface plane. No rotation of the deposition strategy was conducted between layers. After the gun scanned the entire substrate area, a layer was completed. The distance between parallel path lines, step, was 1 mm, and the robot velocity was 0.5 m s^{-1}. The Metal Knitting scanning strategy used a radius of 3 mm, a cone angle of 35 degrees with the virtual cone axis, and a robot linear speed of 0.2 m s^{-1}, resulting in a time elapsed at each point of 0.8 s. The CS gun was tilted, and the movement of the deposition was composed of rotation. A detailed description of the Metal Knitting scanning strategy is presented in previous works.[15,16] For CSAM traditional strategy, two samples were sprayed 5 mm far side-by-side at the same time, one for as-sprayed characterization and another for HT, while for CSAM Metal Knitting, two samples were built in individual depositions.

CSAM traditional strategy part was produced on a 50 mm square plate, looking for the minimum sidewall inclination to build the part. As a result, the traditional strategy produced 221 μm thick layers, requiring 226 layers for a 50 mm height sample and 65° inclined sidewalls, **Figure 1**a, whereas the Metal Knitting strategy resulted in 3600 μm-thick layers, requiring 16 layers for a 58 mm height sample, Figure 1b,c shows a scheme for tensile samples extracted from X-direction, Y-direction, and Z-direction, while Figure 1d presents the tensile sample drawing. For neutron diffraction and NT samples, 30 mm height samples were produced, requiring fewer CSAM-ed layers. The sidewall angle correction for the traditional strategy is presented in Figure 1e and resulted in reducing the sidewall angle from 40 to 5 degrees, applying 25 layers each step. However, OM images of the first and second bonding interface showed partial adhesion, with pores and separation along the previous sidewall and the correction layer interface, Figure 1g. A macrography of the crosssection, showing the different built layers, is shown in Figure 1f.

2.3. Heat Treatment

The HT were conducted in a Hobersal CRN 4–18 furnace without a protective atmosphere. Samples produced by either traditional or Metal Knitting strategies were heated to 1000 °C at a heating rate of 0.25 °C s^{-1}, maintained at this temperature for 1 h, and finally cooled in the furnace. These HT parameters were selected based on their possible positive effect on promoting inter-particular bonding and ductility for CSAM-ed 316L, as presented in previous works.[24–26]

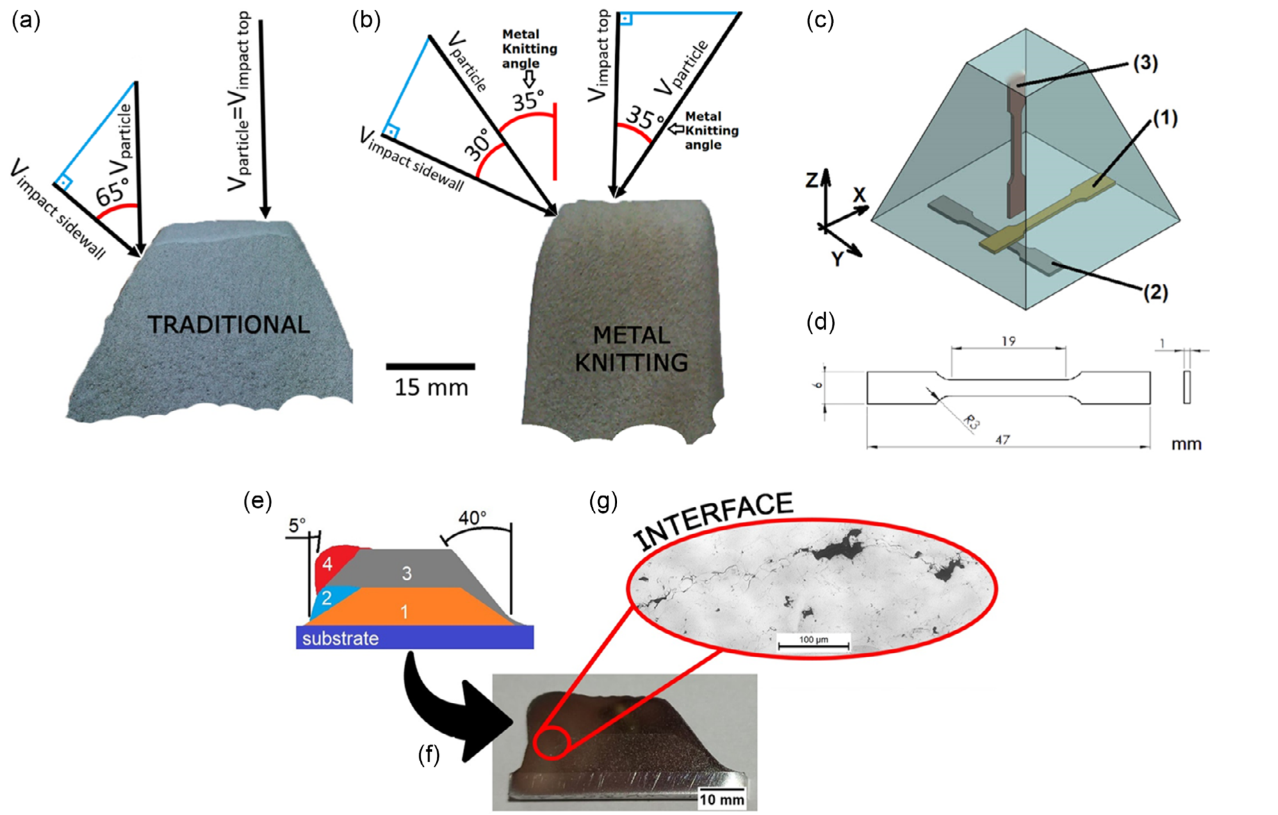

Figure 1. Scheme for velocity of impact (v_{impact}) of particles for different surfaces, using the CSAM a) traditional, and b) Metal Knitting strategies. c) Scheme for tensile samples extracted from X-direction, Y-direction, and Z-direction. d) Tensile sample drawing. The CSAM traditional 316L applying correction sidewall angles layers, showing e) a schematic of deposition layer sequence, f) macrography showing the interlayer region, and g) a micrograph showing the interface layer.

2.4. Characterization and Mechanical Properties Testing

The samples were cut, ground, and polished using a standard metallography procedure and etched by Aqua Regia reagent. A Leica DMI5000M microscope was used for optical microscopy (OM) analysis. Porosity was analyzed with the software ImageJ on five OM images at 200× magnification for each sample, according to ASTM E2109-01 standard.[29] The grain orientation and deformation behavior of CSAM-ed 316L were characterized by the electron backscattering diffraction (EBSD) technique. EBSD data were treated with MTEX open source package.

Microhardness was measured utilizing Shimadzu HMV equipment, applying a load of 0.3 kgf ($HV_{0.3}$), resulting in average values of 10 indents in the Vickers scale for each point of interest. Following the Figure 1c scheme, the microhardness was measured at seven samples' Z-direction heights, i.e., distance from the substrate interface in Z-direction, with two orientations at each Z distance: the XY-plane (seven samples) and XZ-plane (single sample).

Three samples in each direction were fabricated by wire electrical discharge machining process for tensile testing, following the drawing in Figure 1c–d. The surfaces were polished to a maximum roughness of Ra 0.8 μm and a ZwikRoell Zmart. Pro equipment with an Xforce P 10 kN load cell was used for the tensile testing, with a load application velocity of 1.0 mm min^{-1}. The fractography was performed using SEM images in the backscattered electron mode of the fracture surfaces.

2.5. Neutron Tomography (NT)

The NT measurements were performed on the imaging beamline Dingo at ANSTO.[30] The instrument was configured in high-resolution acquisition mode, corresponding to an L/D ratio of 1000, where L is the distance between the beam collimator to the image plane, and D is the diameter of the collimator. The ZWO CMOS ASI2600MM Pro (6248 × 4176 pixels) was coupled with a 50 mm lens to yield images with a pixel size of 36 μm over a 224 × 150 mm^2 field of view. The detector system had a 50 μm thick $^6LiF/ZnS$ scintillation screen. Projections were acquired with an equiangular step of 0.19° over 360° and an exposure time of 70 s each. Flat field normalization with dose correction, dark current subtraction, ring artifacts suppression in frequency, and real space domains were applied to each dataset. The NT stacks were computed using the NeuTomPy toolbox.[31] The ThermoFisher Avizo 2020.3.1 software was employed for data visualization and evaluation.

2.6. Residual Stress Measurement

Residual stress measurements were conducted using the stress diffractometer KOWARI at the ANSTO OPAL research reactor.[32] The stress intensity and distribution were performed in conditions optimized for γ-Fe {311} reflection at the wavelength of 1.55 Å, when the scattering angle was close to the optimal 90°-geometry with the take-off angle of 69° using a Si {400} monochromator. A cube-like gauge volume with dimensions $5 \times 5 \times 5\,mm^3$ was provided employing the focusing collimator. With this gauge volume, 2D meshes with 55 to 67 points were chosen congruent to the size of the gauge volume with 4 mm steps in the two dimensions. All measurement points were taken so the gauge volume was always fully submerged in the material, with a strain accuracy of 70 microstrains. The achieved experimental uncertainties were $\approx$10 MPa, which resulted from the strain accuracy of 50 microstrains (5×10^{-5}). For stress calculations from the measured strain, the (*hkl*) dependent isotropic elastic diffraction constants were used and evaluated under corresponding single crystal elastic constants using ISODEC software.[33]

3. Results

Previous to the CSAM deposition, the 316L feedstock powder was characterized. The chemical composition indicates that the material followed the ASTM A240/A240M standard[34] for the 316L stainless steel, with composition Fe-16Cr-12.3Ni-2.6Mo-0.5Mn (in wt%). The 316L feedstock powder presented an irregular shape and a particle size distribution of 60 μm for d_{90} and 15 μm for d_{10}, with an average value of 31 μm, as previously shown by Vaz et al.[27] and added as Figure A–B, Supporting Information.

3.1. Microstructural Characterization

Figure 2 shows OM images of the samples on the XY-, YZ-, and XZ-plane, following the references presented in Figure 1c. All the samples showed metallic phase, pores, and the absence of oxide layers between the particles, a typical feature of a CSAM-ed material. As the feedstock powder used was water-atomized with an irregular shape, as presented by Vaz et al.[27] the flattening ratio was not measured since it compares the initial powder spheroidicity with the deformed particles.

By a visual inspection and image analysis measuring the porosity, no densification was observed as an effect of the HT. In the as-sprayed condition, both CSAM strategies resulted in micropores remaining in the inter-particular region, i.e., micropores or microvoids between the particles that are not observed in OM images. These microvoids in the inter-particular regions are presented in SEM image shown in Figure 2e. Besides the inter-particular region, Figure 2e indicates by arrows points of micro-welding between the particles; however, just a few points have this strong bonding link, and non-metallurgic consolidation mechanisms predominate for CSAM-ed material. More large porosity is observed for CSAM Metal Knitting samples as a lower particle deformation than for the CSAM traditional 316L, which is a consequence of the lower impact velocity imposed by the Metal Knitting strategy.

CSAM samples show an apparent increase in porosity after HT, as seen in Figure 2. However, this is not reflected by the porosity value by image analysis, which only increased from 4.1 ± 1.5 to $4.3 \pm 0.5\%$ after HT and from 7.5 ± 4.6 and $7.7 \pm 3.3\%$ after HT for CSAM traditional and Metal Knitting, respectively. The pore size distribution is presented in Figure F, Supporting Information. All four histograms had an asymmetrical and left-skewed distribution, indicating a prevalence of small particles in the microstructure and a few large pores, confirming the microstructural image observation in Figure 2. It shows a higher quantity of small pores, $< 0.2\,\mu m^2$ for

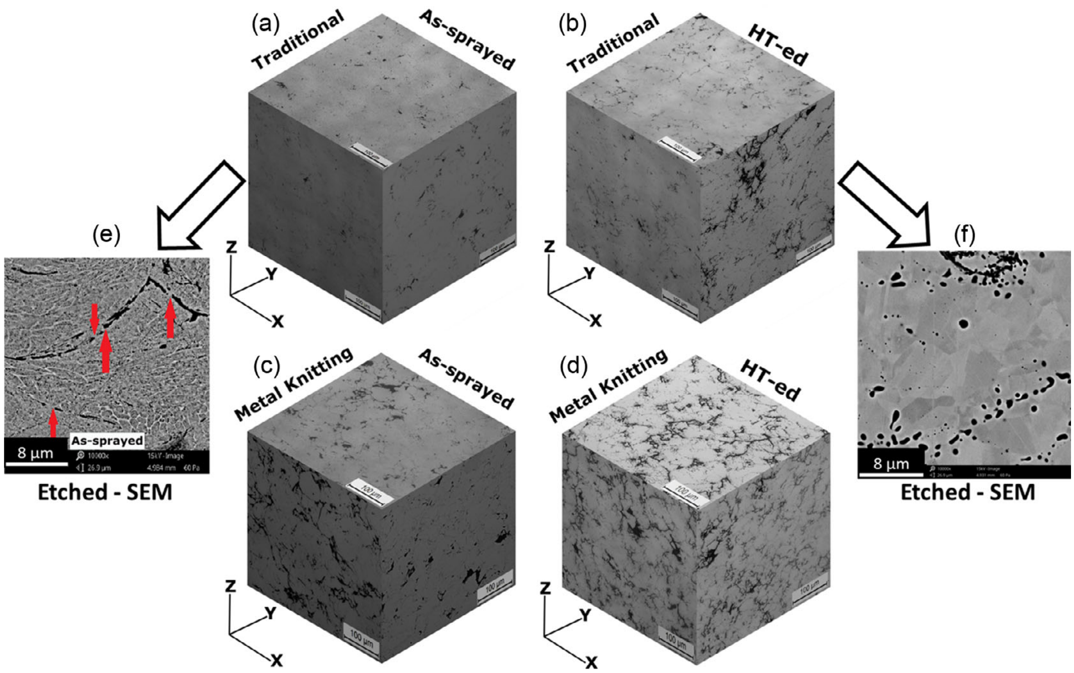

Figure 2. CSAM traditional and Metal Knitting 316L microstructures. OM images a,c) before, and b,d) after HT. SEM images of etched CSAM traditional 316L e) before, and f) after HT. OM scalebar: 100 μm, SEM scalebar: 8 μm.

CSAM traditional than for Metal Knitting in as-sprayed. For the CSAM traditional sample, HT increased the frequency of $< 0.1\,\mu m^2$ pores, while for CSAM Metal Knitting, HT diminished the $< 0.1\,\mu m^2$ pores and increased the frequency of pores > 0.4 and $< 2.0\,\mu m^2$. The increase in the number of small pores and medium-sized pores amount, for traditional and Metal Knitting strategies, respectively, is a result of the coalescence of smaller pores into larger pores due to the diffusional mechanism, which allows their mobility between the particles, following the inter-particular path. The coalesced pores can be observed accumulating in the HT-ed sample, Figure 2 (Etched SEM), which was previously the inter-particular region of the as-sprayed material.

Figure 3 depicts the band contrast map of both CSAM strategies, showing as-sprayed and HT-ed conditions. The microstructures are EBSD maps based on band contrast information. Both CSAM strategies in as-sprayed conditions present microstructures with a high deformation degree, leading to regions of low band contrast. These regions represent porosity (absence of EBSD information, leading to the black color) or high dislocation density regions (darker gray areas due to low band contrast), which come from very diffuse backscatter Kikuchi diffraction patterns. After the HT at 1000 °C for 1 h, the interparticular region disappeared, revealing a grain size and distribution uniformity.

Figure 4 presents grain orientation spread (GOS) contrast maps for CSAM traditional and Metal Knitting 316L, as well as for these conditions after the HT. The white areas in these maps refer to nonindexed areas, which were disregarded in the calculation. In summary, GOS values are the mean misorientation values inside a grain, and more information was provided by Allain-Bonasso et al.[35] Here, a grain boundary was defined with misorientation equal to or higher than 15°. It can be noted that as-sprayed samples present high GOS values, achieving values as high as 10°. It indicates a high degree of misorientation due to a strong deformation. It was not observed differences between both CSAM strategies. After HT, lower GOS values indicate recrystallization and a decrease in misorientation. Interestingly, GOS values appear to be higher for Metal Knitting, showing that the recrystallization was more pronounced in the traditional HT-ed sample.

Histograms of geometrical necessary dislocations (GND) were obtained from the same EBSD analyzed area and are depicted in **Figure 5**. Similar GND distribution was found for both conditions, before and after HT. GND mean values obtained were 1.54×10^{15} and $1.74 \times 10^{15}\,m^{-2}$ for as-sprayed CSAM traditional and Metal Knitting strategies, respectively. On the other hand, great GND reduction was obtained after HT, where the highest reduction was observed for CSAM traditional strategy, achieving a mean value of $3.55 \times 10^{14}\,m^{-2}$, while the HT led to a GND reduction to $8.48 \times 10^{14}\,m^{-2}$ for CSAM Metal Knitting 316L.

Figure 6 presents NT single shots scanned from all the CSAM-ed 316L volumes. Differences in gray tone shown in the images reveal variations in the material density or attenuation power. A

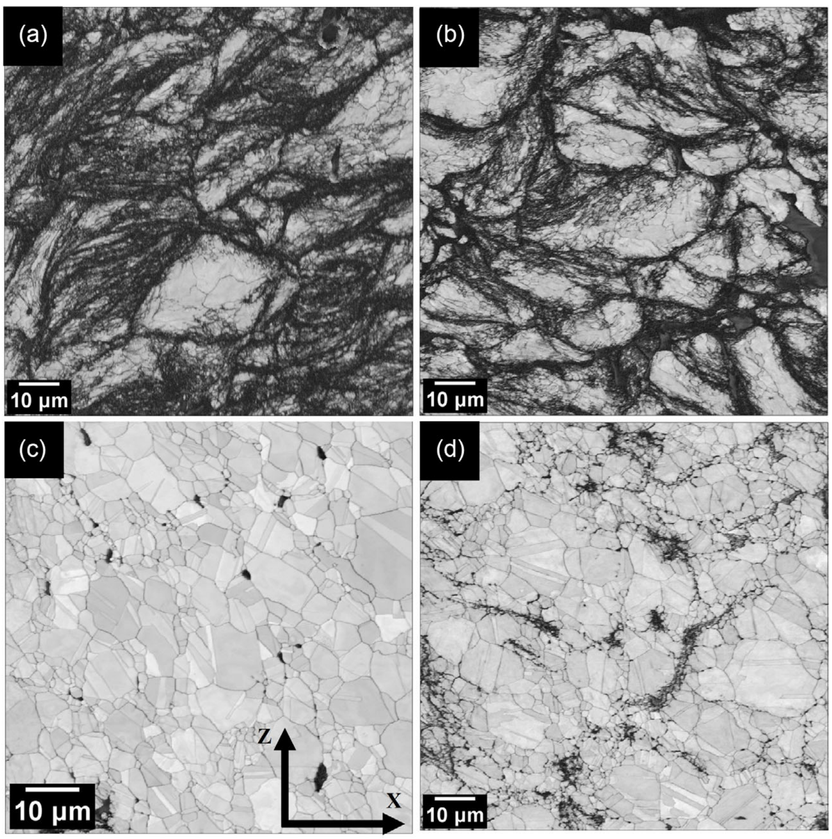

Figure 3. Band contrast EBSD information depicting the microstructure of a–c) traditional, and b–d) Metal Knitting strategies. a–b) As-sprayed and c–d) after HT microstructures.

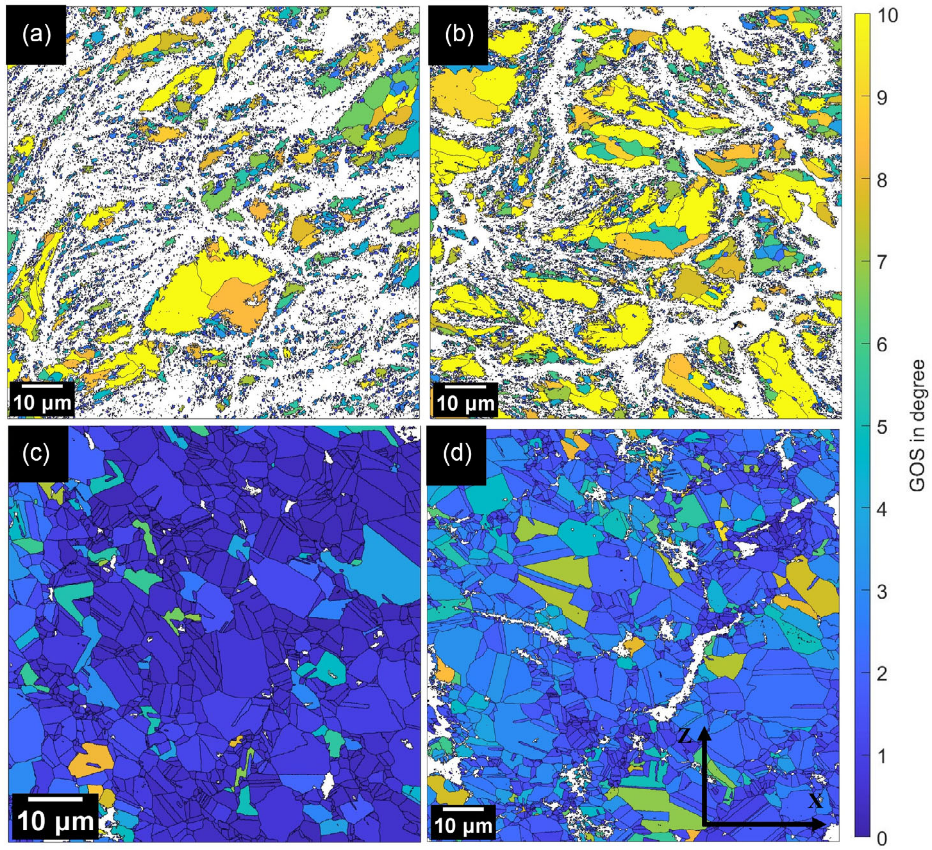

Figure 4. Grain orientation spread for the CSAM a,c) traditional and b,d) Metal Knitting 316L a,b) before and c,d) after HT.

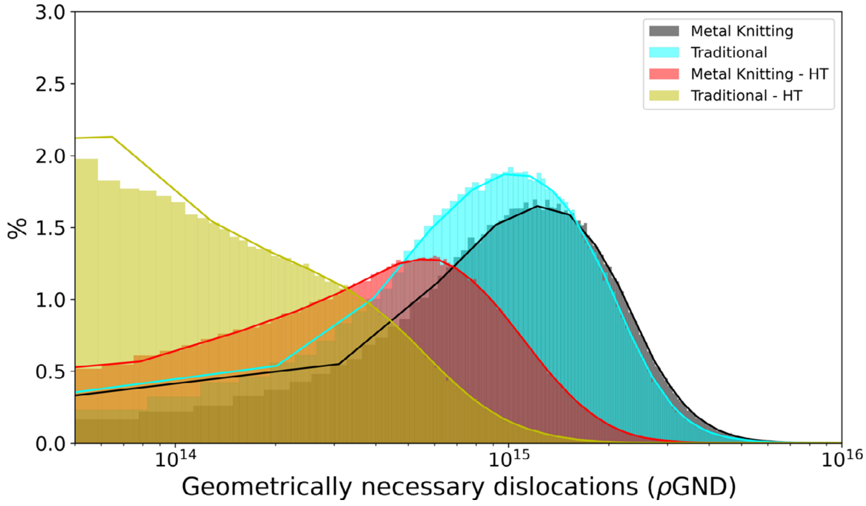

Figure 5. Histograms of geometrical necessary dislocations (GND) values obtained from the same EBSD measured depicted in Figure 3 and 4. Solid lines represent kernel density estimations.

commonality observed in all investigated samples is the absence of coarse porosity, cracks, delamination between the CSAM-ed layers, or another volumetric defect in the materials. NT did not reveal the tiny pores observed in SEM analyses, Figure 2e, f. Visible variation in neutron attenuation (or gray tone) in the NT data can be related to the concurring effect of variation in particle cohesion and porosity below the detection limit. In the as-sprayed CSAM traditional 316L sample, Figure 6, it is possible to see four horizontal bands on the YZ- and XZ-planes. These bands coincide with three moments when the CS

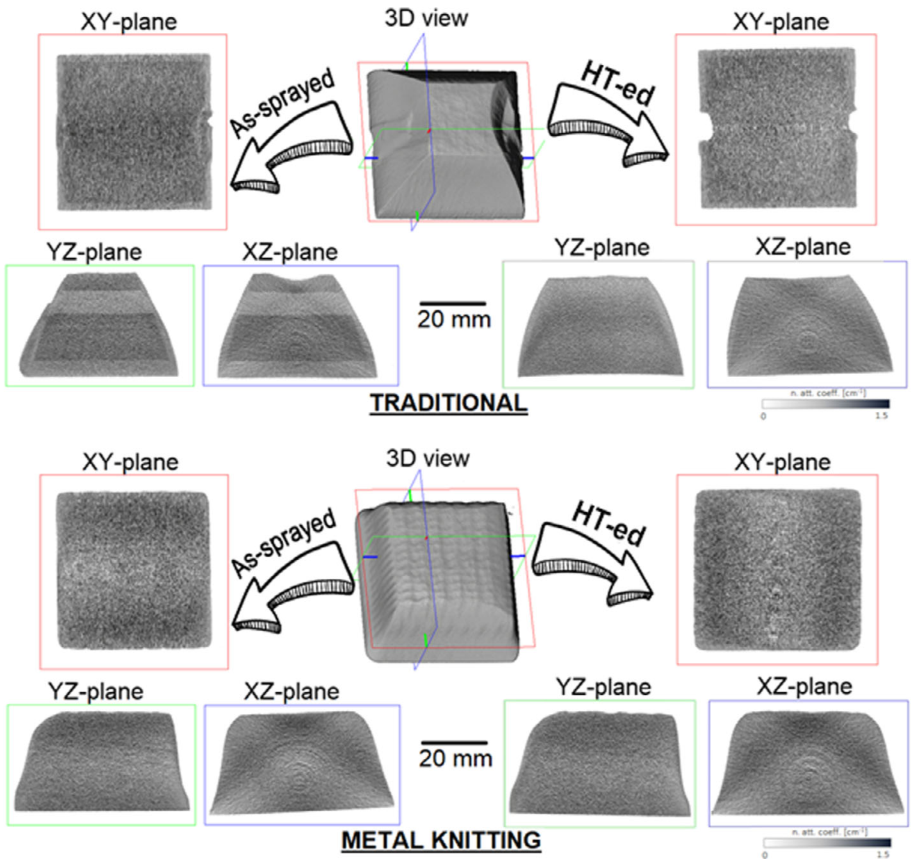

Figure 6. Orthogonal cross sections through the neutron tomography reconstructed volume of CSAM traditional (top) and Metal Knitting (bottom) 316L samples are shown. At the center, the reconstructed three-dimensional models indicate the position of the cross sections. The images of each model's left and right sides refer to the sample as-sprayed and after HT, respectively.

deposition stopped to refill the powder feeder reservoir. Still, no microstructural or porosity differences were observed in OM images of these areas. Band marks did not occur for CSAM Metal Knitting deposition because these pauses were unnecessary due to the thicker layer produced in each pass. Furthermore, Figure 6 indicates that the HT eliminated this horizontal transition, generating a homogeneous NT image color.

3.2. Microhardness Evolution

Figure 7 presents the microhardness results at different distances from the substrate interface, before and after the HT for both CSAM strategies. It compared the direction of measurement perpendicular and parallel to the spraying jet axis XY- and XZ-plane, respectively, per the reference indicated in Figure 1c. For both strategies, no relation to $HV_{0.3}$ to Z position in the specimen was found. However, on the XY-plane, it was shown a slightly higher mean value than on the XZ-plane. For the CSAM traditional 316L as-sprayed, the values measured were 347 ± 28 $HV_{0.3}$ on the XZ-plane and 377 ± 22 $HV_{0.3}$ on the XY-plane; while for the CSAM Metal Knitting, they were 216 ± 46 $HV_{0.3}$ and 246 ± 33 $HV_{0.3}$, respectively. Samples produced by the CSAM traditional strategy presented a great reduction in microhardness on both analyzed planes. At the same time, no significant variation was found in CSAM Metal Knitting 316L with the HT.

Figure 7 also presents indents on samples before and after HT. Those characteristics were seen for all indents performed on the XY- and XZ-plane. Diamond-like marks with no cracks or micro-cracks on or near their corners were obtained for the CSAM traditional strategy samples. Nevertheless, some delamination or decohesion of particles was observed for some indents on CSAM Metal Knitting 316L samples. The indents that resulted in the decohesion of particles were considered invalid to calculate the hardness mean values; however, they indicate qualitatively a lower cohesion of particles and material strength. This decohesion phenomenon was not observed in HT-ed samples, bolstering cohesion improvement by the HT. In addition, for both strategies, marks with a bit of deviation from the perfect diamond-like shape and deformation pile-up in the indent vicinity were not evidenced in the marks observed on HT-ed samples, which can be attributed to the higher plasticity and ductility.[36,37]

3.3. Tensile Properties

Figure 8 shows the ultimate tensile strength (UTS) values measured for the CSAM traditional and Metal Knitting strategies before and after HT. In the as-sprayed condition, the CSAM traditional strategy resulted in higher UTS than the Metal Knitting strategy in all evaluated directions. Additionally, the applied HT

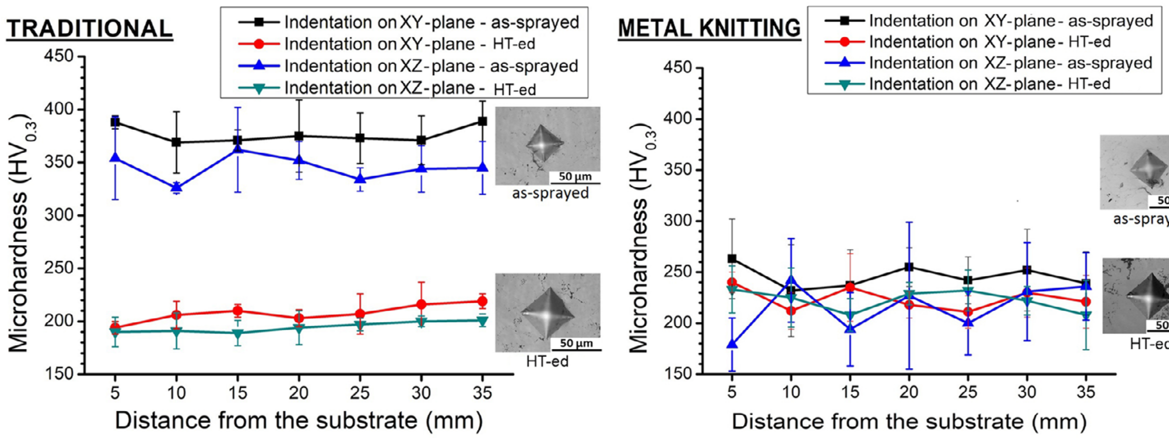

Figure 7. Microhardness profile of CSAM traditional and Metal Knitting 316L as-sprayed and after HT.

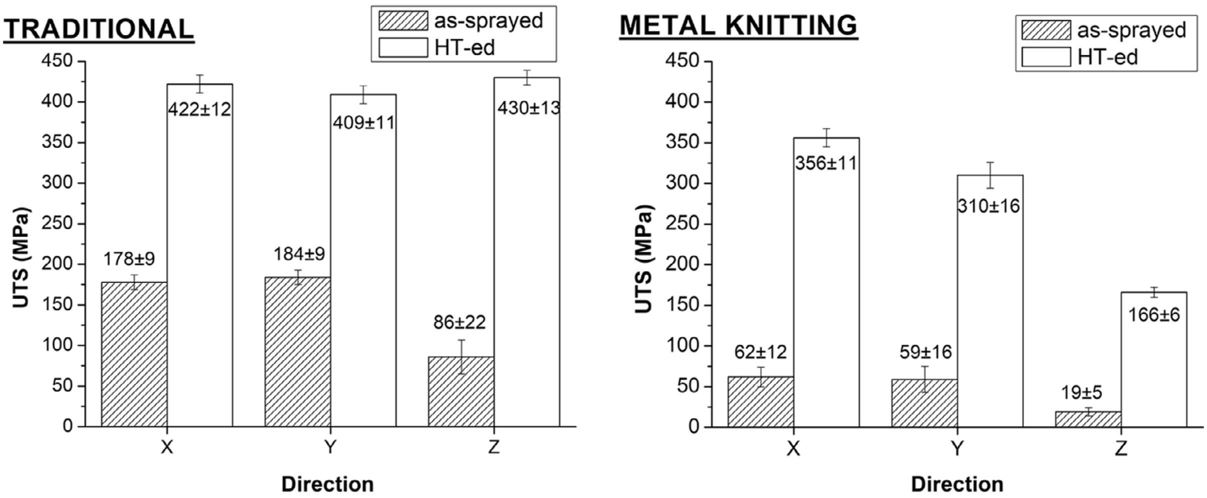

Figure 8. Results of tensile testing of CSAM traditional and Metal Knitting 316L samples as-sprayed and after HT.

increased the UTS for all conditions analyzed, where higher values were obtained for samples produced by the traditional strategy.

There is a clear isotropy in the X- and Y-directions for the traditional and Metal Knitting strategies samples, indicating homogeneity of particle deformation for these axes, which other authors did not observe.[7,38,39] To evaluate the planar isotropy qualitatively, an index UTS_y/UTS_x was plotted, as shown in **Figure 9**. This figure also presents representative results from other authors using different AM strategies, processes, materials, and HT.

The CSAM as-sprayed samples presented in-plane isotropy, $UTS_y/UTS_x \approx 1$, higher than Cu[40] or 316L steel[41] cold worked, due to a preferential direction of grains deformation for this fabrication process higher than the observed for CSAM. The results are similar to the CSAM and selective laser melting (SLM) 316L samples,[42–44] which melts the feedstock powder during the AM part building. The out-of-plane isotropy was lower with UTS_z/UTS_x of 0.48 and 0.31 for CSAM traditional and Metal Knitting strategies, respectively.

For the CSAM traditional strategy as-sprayed, UTS_z/UTS_x was 0.48, while for the Metal Knitting, it was 0.31, which one more time confirms a higher cohesion of particles in the CSAM traditional samples. It is important to note that SLM samples are difficult to compare with CSAM; however, they are AM techniques that have to be compared. The anisotropy for the different AM processes origins from different reasons: for CSAM, the uneven particle plastic deformation at the impact generates lower cohesion of particles in one direction than in another; for SLM, due to the feedstock powder melting, the deposit experiments a directional solidification, a texture, heating and cooling each layer, a thermal history, and tensile residual stress between the layer. Li et al.[45] and Gebisa and Lemu[46] presented AM strategy optimization to improve the AM material isotropy and design of the AM part building, enrolling an unavoidable anisotropy. Considering that CSAM and SLM result in a direction with higher strength in as-built condition, the manufacturers can design a favorable strategy to develop the CS gun or SLM heat source path. However, the AM part use loadings must be known previously.

The HT process improved the UTS for all the samples, CSAM strategies, and directions, as seen in Figure 8. A highlight for the UTS_z had increased its value by five and almost nine times for the CSAM traditional and Metal Knitting strategies, respectively.

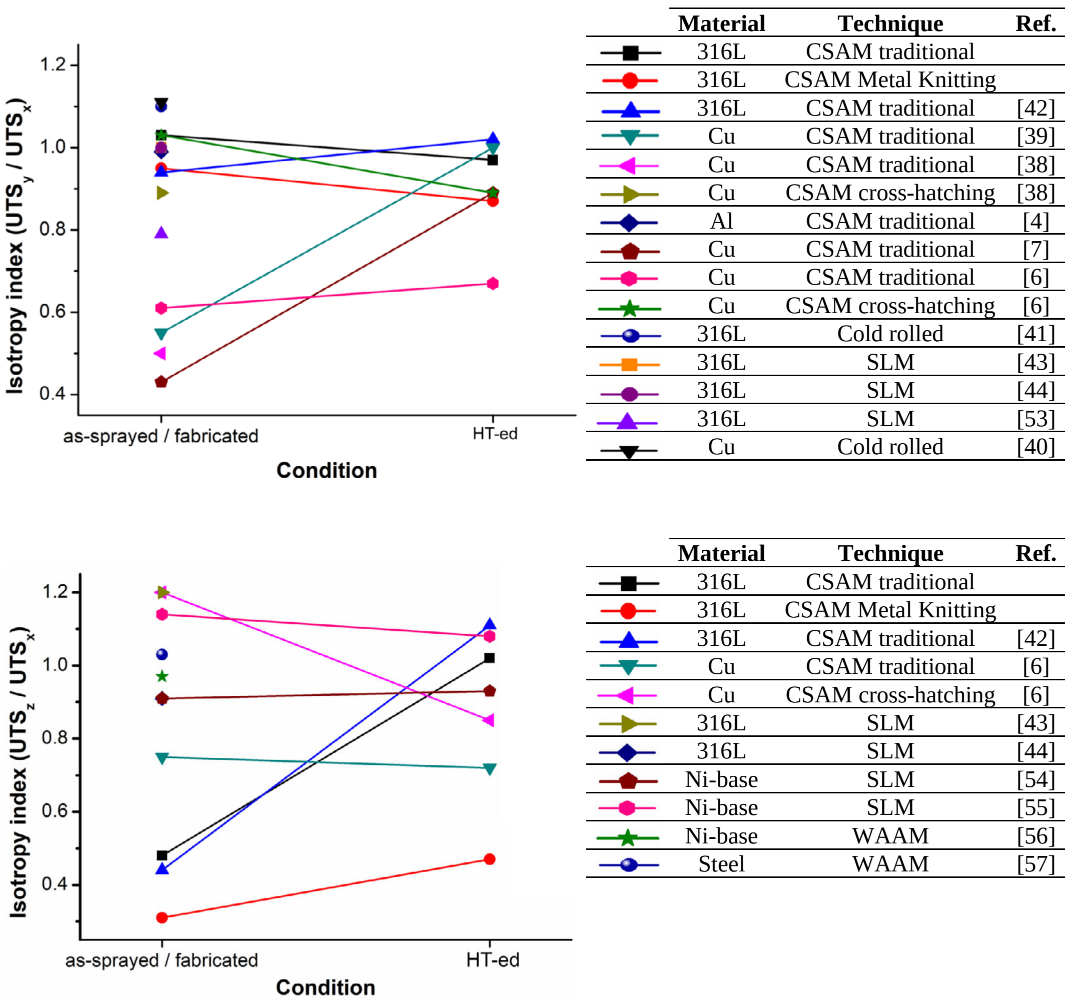

Figure 9. Effect of AM technique, AM strategy, and HT on the material isotropy.

The HT-ed samples presented higher isotropy than the as-sprayed samples, as presented in Figure 9. For the planar isotropy or index UTS$_y$/UTS$_x$, the CSAM traditional and Metal Knitting parts were close to 1.0, the perfect isotropy. However, regarding the index UTS$_z$/UTS$_x$, the Metal Knitting samples had this index improved from 0.31 to 0.48. In contrast, the traditional sprayed samples changed it from 0.48 to 1.02, reaching the isotropy with the X- and Y-directions.

For both CSAM strategies studied, the fracture morphology was observed by SEM to investigate the characteristics and properties of fracture. **Figure 10** shows representative images of the fractures. For both CSAM strategies, the fracture surfaces were identical: the as-sprayed samples had fractures occurring by decohesion of particles, and the fracture surfaces of the HT-ed samples revealed many dimples, indicating the emergence of the ductile mechanism of fracture.

3.4. Residual Stress

The experimental stress maps of the two stress components, $\sigma_{\mathrm{Transversal}}$ and $\sigma_{\mathrm{Longitudinal}}$ in the CSAM-ed 316L, are shown in

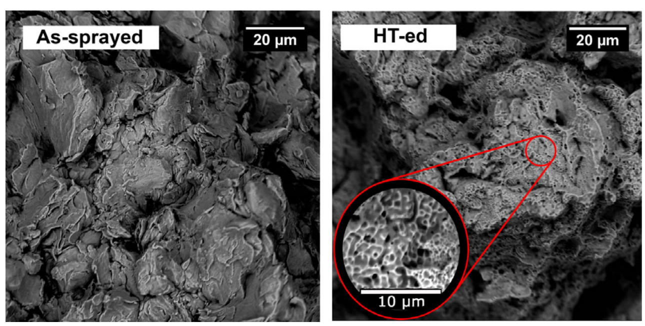

Figure 10. SEM images of the fracture surface of CSAM traditional 316L tensile Z-direction sample as-sprayed and after HT.

Figure 11. The maps interpretation must consider the experimental uncertainties of ≈10 MPa, while the stress values are at ± 100 MPa. Through stress component $\sigma_{\mathrm{Longitudinal}}$, which is integrally balanced to zero in the whole XZ cross- section, Figure 11, it is noticed that the CSAM-ed 316L samples in the as-sprayed condition have their surfaces characterized

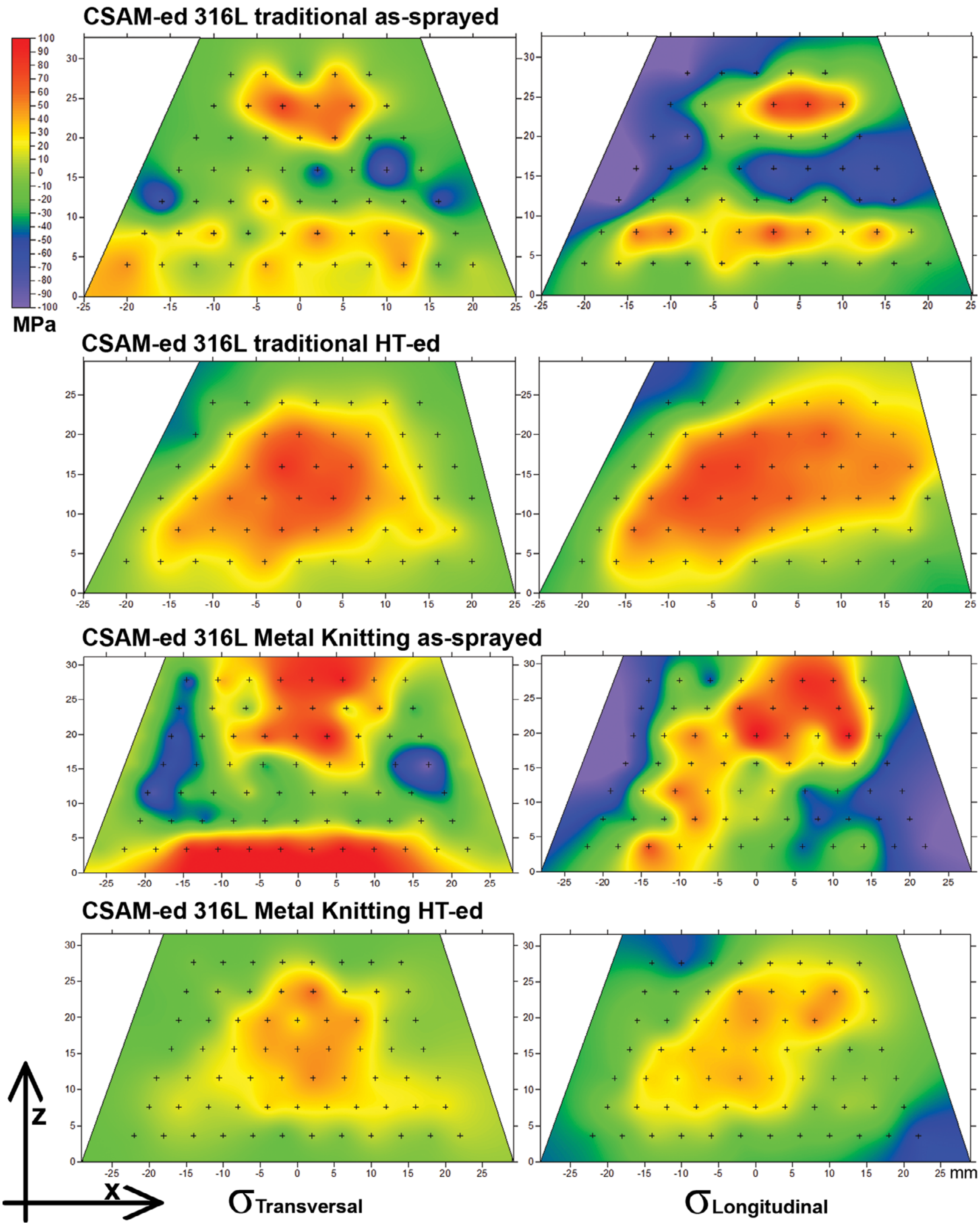

Figure 11. Residual stress distribution in the XZ-plane cross section for CSAM tradi4,7,6tional and Metal Knitting 316L samples as-sprayed and after HT. Two stress components are presented: $\sigma_{Transversal}$ (left column) and $\sigma_{Longitudinal}$ (right column).

mainly by a compressive stress condition, except on a region on the top area of the CSAM Metal Knitting as-sprayed sample.

The alternative HT post-processing resulted in a homogenization of residual stress in the CSAM-ed 316L for both traditional and Metal Knitting deposition strategies, as interpreted from the mappings presented in Figure 11. These mappings of HT-ed samples showed a low magnitude tensile residual stress in the center of the sample and a low compressive stress on their surfaces.

4. Discussion

4.1. Influence of CSAM Strategy on the Velocity of Impact of Particles

The deposition efficiency and the CSAM-ed material consolidation result from the kinetic energy of the particles that is converted into plastic deformation at their impact onto the substrate. The deposition window for 316L steel is between 500 and 675 $\mathrm{m\,s^{-1}}$[47] because particles under the v_{cr} (critical velocity) do not adhere to the substrate. In contrast, particles with an excessive velocity erode the substrate.

In CSAM traditional strategy, with the impact of the particles at 90°, the velocity is parallel to the direction of the particles without subcomponents (624 $\mathrm{m\,s^{-1}}$). This is the $v_{\text{impact top}}$ for the CSAM traditional strategy shown in Figure 1a. However, for its 25° inclined sidewall, the vector velocity responsible for the particle deformation ($v_{\text{impact sidewall}}$) is only 263 $\mathrm{m\,s^{-1}}$ (624 × cos 65°). This velocity is below the v_{cr} for 316L steel (500 $\mathrm{m\,s^{-1}}$),[47] making the material consolidation unfeasible by adiabatic shear instability (ASI) on this CSAM part sidewalls. Nevertheless, employing the novel CSAM Metal Knitting strategy with a knitting angle of 35°, the v_{impact} varies between 511 and 540 $\mathrm{m\,s^{-1}}$, where these are the $v_{\text{impact top}}$ and $v_{\text{impact sidewall}}$, respectively, also shown in Figure 1b. These values are in the deposition window for 316L but very close to the v_{cr} of 500 $\mathrm{m\,s^{-1}}$, resulting in a predictable lower particle deformation but a feasible material anchoring.

4.2. Microstructure Development

The CS-ed particles are severely cold-worked, which acts as the driving force for recrystallization. This energy for recrystallization arises from the lattice strains and the crystalline imperfections and dislocations generated in the material during the CS deposition process.[48] Besides the deformation at the impact, the consolidated CSAM-ed material is exposed to more cold work by the impact of the sequent sprayed particles, known as the shot peening effect.[21,49] The material characteristics change by HT resulted from diffusion mechanisms, which occur due to the temperature above the 316L recrystallization level for enough time to promote atomic movement in the crystalline structure. Therefore, a short annealing time is feasible for CSAM-ed 316L due to the stored energy in the cold deformed particles. In addition, the atomic diffusion improved the cohesion of particles in the regions intimately close to the ASI bonding mechanism, promoting a micro-welding between the particles.

EBSD maps reaffirmed the microstructure evolution due to the HT of CSAM-ed 316L. For the traditional and Metal Knitting strategies, the as-sprayed condition presented severely deformed grains in the surface of the particles, which was altered by the recrystallization and diffusion phenomena during the HT, resulting in equiaxed grains microstructure with small grains in the previous interarticular region. It evidences a material recovery and recrystallization but not a grain coarsening. The coarsening and grain growth should occur for a longer HT; however, keeping small grains is favorable to improve the material mechanical properties, mainly because the grain boundaries act as barriers for the dislocation movements, improving the material strength and hardness.

The lower microhardness for the Metal Knitting condition is evidence of their lower cold working, corroborating the higher porosity discussed previously. Furthermore, it is related to a lower velocity of particles at the impact since the lower the velocity, the lower the kinetic energy converted into plastic deformation. For a flat surface, i.e., the first CSAM layer, this reduction of the velocity of particles, and consequently their kinetic energy, is due to the decomposition of the vector velocity by the cosine of the Metal Knitting angle selected (35°), resulting in a reduction of 27% in velocity. However, from the second layer onward, the previously consolidated CSAM-ed material is no longer a flat surface. This behavior occurs because the metal knitting angle becomes favorable to adhere the CS-ed particles to this curved surface, even with a decomposed vector velocity. On the other side, the similar GOS maps and dislocation density observed for both strategy conditions can be explained by the number of indexed points during measurement, as the high deformation level decreases the fraction of confidence data.

The hardness on the XY-plane was higher because an indent on the XY-plane had a higher probability of obtaining a good hardness value in a deformed grain region in the particles, i.e., a valid mark without cracks, than an indent on the XZ-plane. It happens because the deformed grains are in the particles periphery, and an indention in this zone on the XZ-plane impresses a load that separates or detaches the particles from each other, resulting in an invalid hardness value, which has to be discarded. It obligated the authors to measure the hardness in center of the particles on the XZ-plane, where the cold working is less pronounced and the hardness is lower. This discrepancy of values was more clearly observed for the CSAM traditional strategy due to the higher deformation of particles and cold working produced by the higher velocity of particles in this strategy.

The HT post-process drastically reduced the material hardness for the traditional strategy condition due to the recovery and recrystallization phenomena.[48,50,51] This post-treatment reduced or eliminated the effect of deformation-induced dislocation density, which is typical for the CS-ed particles during their deposition, resulting in a final microhardness between 200 and 250 $\mathrm{HV_{0.3}}$ and reduced GND density for both CSAM deposition strategies (Figure 7), pretty close to the results presented in the literature for HT of CS 316L.[5,24,25,52] After the HT, the hardness on the XY-plane remained higher than the values on the XZ-plane for the CSAM traditional strategy, signing that the recrystallization was not complete by the HT parameters selected, and more than 1 h at 1000 °C is needed for this CSAM-ed 316L size part. For the CSAM Metal Knitting, this trend was not clearly observed due to the lower particle deformation, lower as-sprayed hardness values, and inhomogeneity of microstructure in the same distance from the substrate, interpreted from the high standard deviation values.

4.3. Impact on the Mechanical Behavior

The lower mechanical resistance for the Metal Knitting samples corroborates their higher porosity and lower microhardness measurements previously presented. It is attributed to a lower cold working and particle plastic deformation due to a lower particle kinetic energy resulting from the vector velocity decomposition by the impacting angle of the particles. CSAM is wholly based on particle deformation dependent on the spraying strategy, as seen in the literature for Cu and Al samples.[6,7,38,39,43,53] The CSAM traditional and Metal Knitting 316L resulted in a severe Z/X anisotropy, mainly because of the inhomogeneity of particle deformation in the cited directions, affecting the cohesion of particle mechanisms and making it weaker in the Z-direction than in the X-direction. Furthermore, the contact area between the particles is smaller on the XZ-plane because the particles deform in the jet direction, generating lens-like splats and flattening on the XY-plane, promoting better mechanical anchoring or interlocking on this plane. It does not occur for processes usually applied to produce high-height AM parts, such as SLM or WAAM, where different adhesion mechanisms are active.[43,44,54–57] For CS, the literature presents different bonding mechanisms and considering the particles impacting direction, these mechanisms act favoriting the shear stress resistance. This higher strength is parallel to the substrate plane, XY-plane in Figure 1c. The mechanisms dependent on the particle's high velocity are listed by Vaz et al.[27]: i) ASI; ii) jetting; iii) local melting; iv) mechanical interlocking; v) interfacial mixing; and vi) diffusion.

Tensile samples were designed to guarantee the plane strain, and the literature shows that for a ductile bulk material, the fracture mechanism is the plastic deformation by shear stress in the material under external axial loading, resulting in a fracture angled 45° with the sample symmetry axis.[58] However, all the CSAM-ed 316L as-sprayed had the fracture perpendicular to this symmetry axis and with the crack following the interparticular path, confirming this as the weakest region for the as-sprayed condition samples. Furthermore, it evidences and confirms the weak interface region observed in YZ- and XZ-plane NT images of the traditional sample presented in Figure 6, seen by horizontal lines 5 and 25 mm height in Z-direction. These transition lines coincide with the fracture path observed in tensile testing and are related to CSAM traditional deposition stops for refilling the powder feeder. This refilling stopping was not needed for CSAM Metal Knitting because this strategy and no transition lines were observed in Figure 6. CSAM Metal Knitting resulted in higher layer thickness, needing fewer layers for a 50 mm height deposition.

The decohesion of particles fracture morphology found for as-sprayed samples means detaching particles from their neighbors, also known as inter-particular or fracture. It confirms that the interface between them was the preferential crack-growing path and that this inter-particular area was the weakest region of the material. On the other side, the ductile fracture found for HT-ed samples is a consequence of results from a higher cohesion of particles that results from the micro-welding phenomena by the atomic diffusion mechanism in the interparticular region. This improvement is numerically confirmed by the UTS results presented in Figure 8. Besides the dimples, for the CSAM Metal Knitting samples, large interconnected defects or pores were observed, which represent regions of weaker bonding and serve as a potential cause for a lower UTS and cohesion seen for these samples, even after the HT, which did not reduce the porosity.

4.4. Generated Residual Stress

It is possible to consider two sources of residual stress in the CSAM deposits. One is the interaction between the deposit and the substrate. The second is due to the deposition process that results in the specific stress distribution in the deposit itself when the substrate is separated. This approach of decomposition of the overall stress was used previously.[21,59]

Considering the contribution due to the substrate–deposit interaction, the corresponding stress can be significant or even dominant when the coefficient of thermal expansion mismatch of the substrate and deposit material is great enough. Luzin et al.[20] presented a case for a relatively thick Ti deposit on steel and Al substrate by CSAM, with the CTE mismatch stress being 10 times higher than the deposition stress. The second way of the substrate–deposit interaction arises from the fact that the substrate plays the role of constraint when layers are deposited on it and, therefore, takes part in the overall stress distribution. Suppose the layer is deposited on the substrate with a typical CS compressive stress, as a result, the substrate acquires some tensile stress and gets a concave bending to equilibrate the overall forces and moments. In the case studied in this work, CSAM traditional and Metal Knitting 316L, the 3 mm-thick Al substrate bents a little with inward (concave) curvature during the CS deposition of the first layers, relieving the dominance of the peening effects over the CTE related effects. Similar evidence of compressive residual stress imposed by the peening effect and bonding between the particles was also presented by Nault et al.[10].

When the Al substrates were machined by EDM (with the intent to minimize the impact of the machining process on the CSAM-ed material residual stress) so that the Al substrate does not contribute to the final residual stress distribution, the remaining stress field is only due to the deposition process relieving the CSAM-ed compressive residual stress and peening nature.

Since the deposition stress is the overall result of the composition of the competing quenching and peening mechanisms,[20] it is possible that in some locations where the peening effect is reduced (or quenching effect is increased), the overall deposition stress can have sign changed. In corroboration, Boruah et al.[22] explain that the tensile areas result from the quenching mechanism due to the high energy applied for harder CS-ed particles, like Ti6Al4V or 316L, requiring high gas temperature and pressure (1000 °C and 6 MPa, respectively). In these zones, the quenching mechanism prevailed over the peening one because of the lower velocity of the impact of the particles seen for the CSAM Metal Knitting strategy.

The surface condition is attractive for improving the material performance, reducing the stress concentration and crack nucleation under external loads, as presented by Bagherifard and Gugliano,[60] studying CSAM-ed materials and CS-ed coatings in fatigue testing. Fatigue cracks always nucleate in the areas with concentrated tension, such as surface defects, part geometry, or even excessive roughness, amplified by superficial tensile residual stress.

It is important to notice that the CSAM traditional and Metal Knitting 316L had a surface stress state with a moderate compressive residual stress, favorable for a good performance in the as-sprayed condition. For the CSAM traditional 316L as-sprayed sample, the condition of the particles at the impact favored its higher compressive residual stress by the peening effect, not simply because of the v_{impact} of the particles, which is $624\,\text{m}\,\text{s}^{-1}$ over 511 to $540\,\text{m}\,\text{s}^{-1}$ of the CSAM Metal Knitting ones. Besides that, another factor that corroborates a higher compressive residual stress in CSAM traditional 316L samples was the layer thickness of 221 and 3600 μm for the CSAM traditional and Metal Knitting, respectively. The peening effect, responsible for the compressive residual stress, is limited to a few dozen microns. With this understanding, it is possible to improve the compressive residual stress in CSAM Metal Knitting 316L samples by reducing the feedstock powder feeding or increasing the robot speed to decrease the layer thickness obtained.

Although residual stress distribution after HT might resemble the peening effect in the as-sprayed samples, the nature of these distributions is different. The cooling after HT (with no control cooling rate) resulted in the tensile residual stress in the core part of the sample. In contrast, the outer parts of the deposits gain compressive stress, which is a typical feature of the quenching residual stress distribution.

5. Conclusions

This study analyzed the influence of different CSAM 316L deposition strategies: traditional and Metal Knitting, and the use of HT post-treatment on the CSAM-ed part characteristics and properties. As a result, the following conclusions could be drawn: 1) The CSAM Metal Knitting strategy has better control of the 316L part geometry made than the CSAM traditional strategy, i.e., its sidewall inclination grows vertically or at least under control. In contrast, the CSAM traditional strategy demands correction layers that produce a lower interlayer adhesion. The CSAM Metal Knitting promotes a lower v_{impact} of particles than the CSAM traditional strategy, resulting for 316L a lower microhardness, lower UTS, and higher porosity using that strategy due to the lower kinetic energy of the particles and consequent lower particle deformation; 2) The tensile testing mechanism of fracture is the decohesion of particles or inter-particular for the CSAM-ed 316L in as-sprayed condition. However, the HT improves the cohesion of particles by atomic diffusion and micro-welding, changing the mechanism of fracture to predominantly ductile; 3) CSAM Metal Knitting and traditional strategies produce planar isotropy on the XY-plane; however, anisotropy is evident when contrasting the Z- with X- or Y-direction due to a lower cohesion of particles in the XZ-plane. It occurs because there is a lower occurrence of ASI bonding mechanism resisting the Z-direction loading; 4) Both strategies produced the center of the sample being in tensile residual stress, balanced with a compressive one on the near-surface regions. The magnitude of the residual stress is low, under 100 MPa absolute value. The higher velocity of particles promoted by the CSAM traditional strategy resulted in higher compressive residual stress values than CSAM Metal Knitting due to the higher deformation of particles and peening effect; and 5) The HT relieves the initial residual stress from the deposition process, decreasing the GND density through the recovery and recrystallization phenomena. Although the HT parameters, 1000 °C for 1 h, promote the microstructural changes in CSAM-ed 316L and improve the mechanical properties, the cooling rate in the furnace promotes a quenching effect in the CSAM-ed 316L particular structure, resulting in a moderate final tensile residual stress in the center of the material, < 100 and < 50 MPa for CSAM traditional and Metal Knitting strategies, respectively. Still, the low compressive residual stress prevails in the materials' HT-ed surface.

Supporting Information

Supporting Information is available from the Wiley Online Library or from the author.

Acknowledgements

Grant PID2020-115508RB-C21 funded by MCIN/AEI/10.13039/501100011033 and, as appropriate, by "ERDF A way of making Europe," by the "European Union," or by the "European Union NextGenerationEU/PRTR". Government of Catalonia, SGR 2021SGR00712. R.F. Vaz has a Ph.D. grant from AGAUR, Government of Catalonia, 2020 FISDU 00305. Research Project P13534 accepted at the Australian Centre for Neutron Scattering (ACNS) & National Deuteration Facility (NDF) 2022-1 round. V. Albaladejo and J. Avila are Serra Hunter fellows. This study was financed in part by the Coordenação de Aperfeiçoamento de Pessoal de Nível Superior—Brasil (CAPES)—Finance Code 001. G.G. Ribamar acknowledges partial funding from a CNPq grant.

Conflict of Interest

The authors declare no conflict of interest.

Data Availability Statement

The data that support the findings of this study are available from the corresponding author upon reasonable request.

Keywords

316L stainless steel, additive manufacturing, cold spray, mechanical properties, microstructure, residual stress

Received: December 22, 2023
Revised: April 9, 2024
Published online: April 25, 2024

[1] A. Vargas-Uscategui, P. C. King, S. Yang, C. Chu, J. Li, *J. Mater. Process. Technol.* **2021**, *298*, 117272.
[2] A. Vargas-Uscategui, P. C. King, M. J. Styles, M. Saleh, V. Luzin, K. Thorogood, *J. Therm. Spray Technol.* **2020**, *29*, 1508.
[3] Y. Ren, *Mater. Des.* **2021**, *212*, 110271.
[4] S. E. Julien, A. Nourian-Avval, W. Liang, T. Schwartz, O. C. Ozdemir, S. Müftü, *Eng. Fract. Mech.* **2022**, *263*, 108301.
[5] S. Bagherifard, J. Kondas, S. Monti, J. Cizek, F. Perego, O. Kovarik, F. Lukac, F. Gaertner, M. Guagliano, *Mater. Des.* **2021**, *203*, 109575.
[6] S. Yin, R. Jenkins, X. Yan, R. Lupoi, *Mater. Sci. Eng., A* **2018**, *734*, 67.
[7] K. Yang, W. Li, X. Yang, Y. Xu, A. Vairis, *Surf. Coat. Technol.* **2018**, *350*, 519.
[8] O. Zinovieva, A. Zinoviev, V. Ploshikhin, *Comput. Mater. Sci.* **2018**, *141*, 207.

[9] N. Bastola, M. P. Jahan, N. Rangasamy, C. S. Rakurty, *Micromachines* **2023**, *14*, 1480.
[10] I. M. Nault, G. D. Ferguson, V. Champagne, A. Nardi, *J. Therm. Spray Technol.* **2020**, *29*, 1466.
[11] W. Li, K. Yang, S. Yin, X. Yang, Y. Xu, R. Lupoi, *J. Mater. Sci. Technol.* **2018**, *34*, 440.
[12] R. F. Vaz, A. Garfias, V. Albaladejo, J. Sanchez, I. G. Cano, *Coatings* **2023**, *13*, 267.
[13] A. T. Nardi, T. I. El-Wardany, D. V. Viens, M. E. Lynch, A. Hsu, M. A. Klecka, W. Gu, US 2014/0277669 A1, **2014**.
[14] H. Wu, X. Xie, M. Liu, C. Verdy, Y. Zhang, H. Liao, S. Deng, *Addit. Manuf.* **2020**, *35*, 101356.
[15] R. F. Vaz, V. Albaladejo-Fuentes, J. Sanchez, U. Ocaña, Z. G. Z. G. Corral, H. Canales, I. G. Cano, *Materials* **2022**, *15*, 6785.
[16] A. Garfias, R. Vaz, V. Albaladejo-Fuentes, J. Sánchez, I. G. Cano, *Materials* **2023**, *16*, 4735.
[17] M. Strobl, I. Manke, N. Kardjilov, A. Hilger, M. Dawson, J. Banhart, *J. Phys. D: Appl. Phys.* **2009**, *42*, 243001.
[18] V. Luzin, K. Spencer, M. X. Zhang, *Acta Mater.* **2011**, *59*, 1259.
[19] V. Luzin, K. Spencer, M. X. Zhang, N. Matthews, *Mater. Sci. Forum.* **2013**, *772*, 155.
[20] V. Luzin, O. Kirstein, S. H. Zahiri, D. Fraser, *J. Therm. Spray Technol.* **2020**, *29*, 1498.
[21] V. Luzin, K. Spencer, M. Zhang, N. Matthews, J. Davis, M. Saleh, in *Cold-Spray Coatings* (Eds: P. D. Cavaliere), Springer, Cham, Switzerland **2018**, pp. 451–480.
[22] D. Boruah, B. Ahmad, T. L. Lee, S. Kabra, A. K. Syed, P. McNutt, M. Doré, X. Zhang, *Surf. Coat. Technol.* **2019**, *374*, 591.
[23] T. A. Rodrigues, J. D. Escobar, J. Shen, V. R. Duarte, G. G. Ribamar, J. A. Avila, E. Maawad, N. Schell, T. G. Santos, J. P. Oliveira, *Addit. Manuf.* **2021**, *48*, 102428.
[24] B. Dikici, H. Yilmazer, I. Ozdemir, M. Isik, *J. Therm. Spray Technol.* **2016**, *25*, 704.
[25] B. Al-Mangour, P. Vo, R. Mongrain, E. Irissou, S. Yue, *J. Therm. Spray Technol.* **2014**, *23*, 641.
[26] L.-H. Brassart, J. Besson, F. Delloro, D. Haboussa, F. Delabrouille, G. Rolland, Y. Shen, A.-F. Gourgues-Lorenzon, *J. Therm. Spray Technol.* **2022**, *31*, 1725.
[27] R. F. Vaz, A. Silvello, J. Sanchez, V. Albaladejo, I. G. G. Cano, *Coatings* **2021**, *11*, 168.
[28] R. F. Vaz, A. G. M. Pukasiewicz, G. B. Sucharski, I. B. A. F. Siqueira, S. M. Z. Odake, R. S. C. Paredes, *Int. J. Abras. Technol.* **2021**, *10*, 235.
[29] ASTM, in *E2109-01 – Standard Test Methods for Determining Area Percentage Porosity in Thermal Sprayed Coatings*, ASTM International, West Conshohocken, PA, USA **2021**.
[30] U. Garbe, T. Randall, C. Hughes, G. Davidson, S. Pangelis, S. J. Kennedy, *Phys. Proc.* **2015**, *69*, 27.
[31] D. Micieli, T. Minniti, G. Gorini, *SoftwareX* **2019**, *9*, 260.
[32] O. Kirstein, V. Luzin, U. Garbe, *Neutron News* **2009**, *20*, 34.
[33] T. Gnäupel-Herold, *J. Appl. Crystallogr.* **2012**, *45*, 573.
[34] ASTM, in *A240/A240M-22a – Standard Specification for Chromium and Chromium-Nickel Stainless Steel Plate, Sheet, and Strip for Pressure Vessels and for General Applications*, ASTM International, West Conshohocken, PA, USA **2022**.
[35] N. Allain-Bonasso, F. Wagner, S. Berbenni, D. P. Field, *Mater. Sci. Eng., A* **2012**, *548*, 56.
[36] N. Fan, J. Cizek, C. Huang, X. Xie, Z. Chlup, R. Jenkins, R. Lupoi, S. Yin, *Addit. Manuf.* **2020**, *36*, 101626.
[37] J. Ajaja, D. Goldbaum, R. R. Chromik, *Acta Astronaut.* **2011**, *69*, 923.
[38] K. Yang, W. Li, X. Yang, Y. Xu, *Surf. Coat. Technol.* **2018**, *335*, 219.
[39] K. Yang, W. Li, X. Guo, X. Yang, Y. Xu, *J. Mater. Sci. Technol.* **2018**, *34*, 1570.
[40] A. A. Bryukhanov, A. F. Voitenko, V. V. Usov, A. A. Chernyi, *Strength Mater.* **1979**, *11*, 914.
[41] Z. You, H. Fu, S. Qu, W. Bao, L. Lu, *Nano Mater. Sci.* **2020**, *2*, 72.
[42] Y. Yamazaki, H. Fukanuma, N. Ohno, *J. Jpn. Therm. Spray Soc.* **2016**, *53*, 91.
[43] A. A. Deev, P. A. Kuznetcov, S. N. Petrov, *Phys. Proc.* **2016**, *83*, 789.
[44] A. Charmi, R. Falkenberg, L. Ávila, G. Mohr, K. Sommer, A. Ulbricht, M. Sprengel, R. Saliwan Neumann, B. Skrotzki, A. Evans, *Mater. Sci. Eng., A* **2021**, *799*, 140154.
[45] S. Li, S. Yuan, J. Zhu, C. Wang, J. Li, W. Zhang, *Addit. Manuf.* **2020**, *36*, 101406.
[46] A. W. Gebisa, H. G. Lemu, *IOP Conf. Ser.: Mater. Sci. Eng.* **2017**, *276*, 012026.
[47] F. Gärtner, T. Stoltenhoff, T. Schmidt, H. Kreye, *J. Therm. Spray Technol.* **2006**, *15*, 223.
[48] F. J. Humphreys, G. S. Rohrer, A. Rollett, in *Recrystallization and Related Annealing Phenomena*, 3rd ed., Elsevier, Amsterdam **2017**.
[49] Y. Xie, C. Chen, M. P. Planche, S. Deng, R. Huang, Z. Ren, H. Liao, *J. Therm. Spray Technol.* **2019**, *28*, 769.
[50] W. Sun, A. W.-Y. Tan, K. Wu, S. Yin, X. Yang, I. Marinescu, E. Liu, *Coatings* **2020**, *10*, 123.
[51] R. Huang, M. Sone, W. Ma, H. Fukanuma, *Surf. Coat. Technol.* **2015**, *261*, 278.
[52] S. Yin, J. Cizek, X. Yan, R. Lupoi, *Surf. Coat. Technol.* **2019**, *370*, 353.
[53] L. Hitzler, J. Hirsch, B. Heine, M. Merkel, W. Hall, A. Öchsner, *Materials* **2017**, *10*, 1136.
[54] D. Deng, R. L. Peng, H. Brodin, J. Moverare, *Mater. Sci. Eng., A* **2018**, *713*, 294.
[55] D. Tomus, Y. Tian, P. A. Rometsch, M. Heilmaier, X. Wu, *Mater. Sci. Eng., A* **2016**, *667*, 42.
[56] T. Hassel, T. Carstensen, *Weld. World* **2020**, *64*, 1921.
[57] L. Sun, F. Jiang, R. Huang, D. Yuan, C. Guo, J. Wang, *Mater. Sci. Eng., A* **2020**, *787*, 139514.
[58] H. Li, M. W. Fu, J. Lu, H. Yang, *Int. J. Plast.* **2011**, *27*, 147.
[59] R. Sinclair-Adamson, V. Luzin, A. Duguid, K. Kannoorpatti, R. Murray, *J. Therm. Spray Technol.* **2020**, *29*, 1525.
[60] S. Bagherifard, M. Guagliano, *Int. J. Fatigue* **2020**, *139*, 105744.